Influence of defects on the critical behavior at the 105 K structural phase transition of $SrTiO_3$: On the origin of the two length scale critical fluctuations

H. Hünnefeld, T. Niemöller, and J. R. Schneider
Hamburger Synchrotronstrahlungslabor HASYLAB at Deutsches Elektronen-Synchrotron DESY, Notkestrasse 85, D-22603 Hamburg, Germany

U. Rütt
Argonne National Laboratory, 9700 S. Cass Avenue, Argonne, Illinois 60439

S. Rodewald and J. Fleig
Max-Planck-Institut für Festkörperforschung, Heisenbergstrasse 1, D-70569 Stuttgart, Germany

G. Shirane
Department of Physics, Brookhaven National Laboratory, Upton, New York 11973
(Received 5 March 2002; published 26 July 2002)

The temperature dependence of the sharp and the broad component of the critical scattering above the cubic-to-tetragonal phase transition of $SrTiO_3$ has been studied by means of high-resolution triple-crystal diffractometry using 100–200 keV synchrotron radiation in five samples differing with respect to growth technique and oxygen vacancy concentrations. Emphasis is on changes in the critical behavior, the critical temperature, and the strain fields at the transition from bulk to surface. The sharp component was observed only in surface near regions of highly perfect crystals and is coupled to the occurrence of a long-range strain gradient that was identified by an exponential increase of mosaicity, lattice parameter fluctuations, and Bragg-peak intensity when approaching the surface from the bulk of the sample. Vanishing of the sharp component was observed at the polished/etched surface of a platelet cut off the large perfect crystal after release of strain due to free bending of the platelet. The values of the critical temperature observed in the bulk of the different samples vary between $98.7 \leqslant T_c \leqslant 105.8$ K. In the surface near regions of a highly perfect float-zone grown crystal a variation of T_c of about 0.5 K has been found. Concerning the broad component the critical exponent describing the temperature dependence of the inverse correlation length κ_b varies between $0.73 \leqslant \nu_b \leqslant 1.19$, the exponent for the susceptibility between $1.49 \leqslant \chi_b \leqslant 2.9$, however, the ratio of the two exponents is almost sample independent and equal to $\chi_b/\nu_b = 2.1$ with a variance of 0.2, in good agreement with the theoretical value of 1.97 obtained by LeGouillou and Zinn-Justin [Phys. Rev. B **21**, 3976 (1980)]. The occurrence of the sharp component did not affect significantly the critical exponents for the underlying broad component of the critical scattering. The exponents for the sharp component observed in surface near layers of about 100 μm thickness at the highly perfect float zone and flux grown crystals varied between $0.58 \leqslant \nu_s \leqslant 1.30$, the values for the ratio varied between $3.3 \leqslant \chi_s/\nu_s \leqslant 4.6$. The average value of χ_s/ν_s is 3.9 with a variance of 0.5, and is about twice the ratio χ_b/ν_b for the broad component as suggested by Harris *et al.* [Phys. Rev. B **52**, 14 420 (1995)].

DOI: 10.1103/PhysRevB.66.014113 PACS number(s): 61.10.−i, 68.35.Rh, 64.60.−i, 68.35.Dv

I. INTRODUCTION

According to modern theories of phase transitions based on the concept of scaling, the properties of the fluctuations associated with continuous phase transitions close to the critical temperature T_c are determined by a single length scale that varies with temperature. In contrast, high-resolution x-ray diffraction studies of structural phase transitions in perovskites revealed the existence of a second length scale in the critical fluctuations above T_c, which had not been observed in earlier neutron scattering experiments, i.e., in addition to the well-known Lorentzian-shaped scattering distribution a sharp component of Lorentzian squared shape is observed. Later this effect has also been found in magnetic systems. The two length scale problem was discussed by Cowley.[1] The effect was first observed by Andrews[2] at the cubic-to-tetragonal second-order phase transition in $SrTiO_3$ at $T_c \approx 105$ K and the temperature dependence of the two components has been studied by McMorrow *et al.*[3] using 11 keV synchrotron radiation. Shirane *et al.*[4] showed that this sharp component is different from the central peak discovered by Müller and Berlinger[5] and by Riste *et al.*[6] in different studies of the temperature dependence of the soft phonon mode. Later it has been shown that the sharp component originates from regions (<100 μm) close to the surface of the samples[7–9] and is related to the quality of the respective surfaces.[7,10] Wang *et al.*[11] suggested that edge dislocations close to the surface cause the effect. However, the nature of the defects responsible for the sharp component and the role of the surface is not clear yet.

In this paper we present a systematic investigation of the critical scattering in different samples, differing with respect to the growth technique, the degree of crystallographic perfection and the concentration of oxygen vacancies, which has

TABLE I. Specifications of the five different samples investigated.

Sample no.	Growth technique	Sample preparation	Sample color
I	Float-zone grown		Brownish, transparent
II	Flux grown Verneuil grown	Etched (89% H_3PO_4, 1 h, 160 ° C)	Brownish, transparent
III	Oxidized	48 h, O_2 atmosphere, 1 bar, 1000 °C	Rose, transparent
IV	As grown		Transparent
V	Reduced	5 h, H_2 atmosphere, 1 bar, 1250 °C	Black

been determined independently. Surface effects could be separated from the bulk behavior by carrying out diffraction experiments with a flat beam of high-energy photons (100–120 keV), 10 μm in height. In order to clarify the influence of defects on the occurrence of the second length scale in the surface near region the depth dependence of the oxygen vacancy concentration and of crystallographic parameters such as mosaicity, lattice parameter variation, and integrated reflectivity of Bragg reflections has been measured and compared with that of the critical behavior.[12]

The paper is organized as follows. After the description of the experimental setup in Sec. II, the preparation and the characterization of the different samples is discussed in detail in Sec. III. The procedure for determining the critical temperature in the bulk and near the surface of the different samples is presented in Sec. IV. The effect of defects on the critical fluctuations in the bulk of the samples, i.e., on the broad component of the critical scattering distribution, is described in Sec. V. The results of the investigation of the nature of the sharp component in the surface near region are presented in Sec. VI. Finally, the results are discussed in Sec. VII. In Appendix A the mathematical details of the applied procedures to deconvolute the experimental data from the instrumental resolution are described.

II. EXPERIMENTAL SETUP

The scattering experiments have been performed on five different samples using 100 and 120 keV synchrotron radiation at the undulator beamline at PETRA II and the wiggler beamline BW5 at DORIS III at HASYLAB, respectively. All data have been collected at triple-axis-diffractometers in Laue geometry at the position of the (531)/2 superlattice reflection for samples III–V (see Table I) and at the position of the (511)/2 superlattice reflection for sample I and II, respectively. In order to get both, high incident photon flux and adequate **q**-space resolution in the scattering plane, annealed Si crystals diffracting from (311) lattice planes have been used as monochromator and analyzer. The instrumental resolution in the scattering plane has been determined by measuring the superlattice reflection a few degrees below the transition temperature, examples are shown in Fig. 1. It results to $\Delta q_x = 1\times10^{-3}$ Å^{-1} ($\Delta q_x = 1.5$–3×10^{-3} Å^{-1}) at PETRA2 (BW5) in the longitudinal direction [Fig. 1(a)] and 1.6×10^{-4} Å$^{-1} \leqslant \Delta q_y \leqslant 2\times10^{-3}$ Å^{-1} in the transverse direction [Fig. 1(b)], depending on the mosaicity of the respective sample. Perpendicular to the scattering plane the resolution (FWHM, full width at half maximum) was of the order of $\Delta q_z = 2\times10^{-1}$ Å^{-1}. The deconvolution of the experimental data was performed as described by Hirota *et al.*[13] A detailed description of the deconvolution procedure is given in the Appendix. At station BW5 the crystallographic perfection of the samples has been characterized at the (511) main reflection, using perfect silicon monochromator and analyzer crystals diffracting from the (624) lattice planes. The difference in lattice spacing between sample and monochromator/analyzer is $\sim$3.6%. Due to this almost dispersion-free setup the instrumental resolution is improved for the (511) main reflection both in the longitudinal ($\Delta q_x = 1.2\times10^{-4}$ Å^{-1}) and in the transverse direction ($\Delta q_y = 1.0\times10^{-5}$ Å^{-1}).

Due to the high brightness of the high-energy photon beams available at the triple crystal diffractometers at beamlines BW5 and PETRA2 the cross section of the incident beam could be reduced to 10 μm in height and 2 mm in width still allowing a very good peak to background ratio in the measurements of critical scattering. This way the necessary high **q** and high real space resolution could be obtained. The surface of the sample was oriented parallel to the flat beam, the experimental procedure for the alignment of the microslit is given in Ref. 9. By vertical translation of the sample the scattering volume can be moved to well-defined positions in the crystal (see Fig. 2). Due to the special geometry of the samples [the (511) reciprocal lattice vector is almost parallel to the investigated surface and the flat incident beam] the depth dependence of crystallographic quanti-

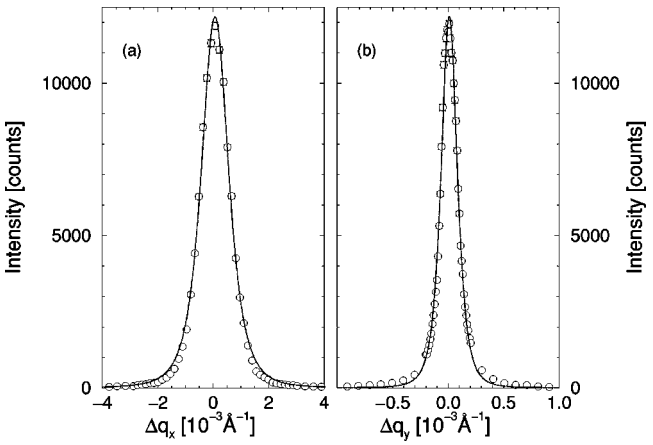

FIG. 1. Longitudinal (a) and transverse (b) scattering profiles of the (511)/2 superlattice reflection of sample I about 2 K below the critical temperature as measured with 100 keV photons at the PETRA II undulator beamline. The solid lines represent the best fits to the data using a Lorentzian-squared profile.

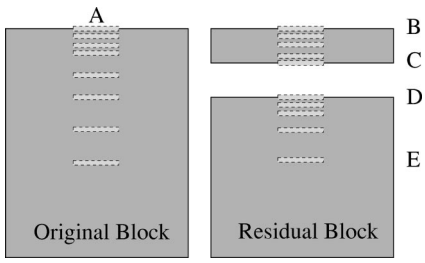

FIG. 2. Schematic drawing of the location of the investigated volume elements of the float-zone grown sample (I). The scattering vector is parallel to the crystal surface. Details of the crystallographic sample orientation are given in the Appendix. The left-hand side shows the original sample investigated by Rütt *et al.* (Ref. 9), the right-hand side shows the 560 μm thick platelet from the top of the original sample and the residual crystal block, the material in between was lost due to polishing and etching the two surfaces. The capital letters A–E define the nomenclature used in this paper. Region A corresponds to the surface of the original block. Regions B and C correspond to the two surfaces of the cut platelet, region D denotes the surface of the residual block, and region E labels the bulk of this block. The lighter rectangles (not to scale) indicate locations of the incident beam with respect to the sample surface. The dimensions of the original sample were about $1\times1\times1$ cm^3, the cross section of the beam was 10 μm$\times2$ mm.

ties such as strain and mosaicity can be studied with a spatial resolution of ~10 μm. In the following, the depth 0 μm corresponds to the sample position, where the complete beam just penetrates the crystal. Consequently, at a depth of -10 μm the beam is just passing the sample. These positions are located by accurately measuring the dependence of the transmitted intensity as a function of the vertical position of the beam in the sample.

III. SAMPLES

The influence of defects on the bulk critical behavior of $SrTiO_3$ has been studied in five samples, differing in growth technique and heat treatment. In order to study the effect of oxygen doping, bulk measurements have been performed on a reduced, an oxidized, and an as-grown Verneuil single crystal. Additionally, a flux-grown sample[14] and an almost perfect crystal, grown by means of the top-seeded float-zone technique,[15] have been investigated. In Table I the different sample treatments and growth techniques are summarized.[16]

The mosaicity of the Verneuil-grown crystals varied between 30 arcsec and 100 arcsec, which is rather broad compared to the almost perfect float-zone grown (1–7 arcsec) and flux-grown samples (10 arcsec). However, the latter two crystals are slightly brownish, perhaps due to iron impurities,[17] in contrast to the transparent as-grown Verneuil samples. In the Verneuil-grown samples the vacancy concentration of the bulk has been determined from conventional impedance measurements of the isolating as-grown and the oxidized samples using vacancy mobility,[18,19] and for the almost metallic reduced samples by means of Hall-resistivity measurements. Interestingly, the amount of oxygen vacancies is about two orders of magnitude bigger for the crystallographic more perfect samples compared to the as-grown and oxidized Verneuil-grown crystals. However, the reduced Verneuil-grown sample shows significant changes: the color changes from transparent to black and the resistance decreases substantially, i.e., the amount of oxygen defects increases by about three orders of magnitude. The depth dependent concentration of the twofold negatively charged oxygen vacancies has been investigated using impedance spectroscopy:[20,21] Following the description given in Ref. 19 microelectrodes of different diameters were used to analyze the depth dependence of the conductivity. Using gold microelectrodes (15–220 μm) the conductivity measured at $\sim200\,^{\circ}$C could be shown to be depth independent in the top 500 μm of both samples I and II. It can therefore be concluded that the vacancy concentration is depth independent as well. Consequently, the sharp component, which has been observed in sample I up to a depth of 100 μm,[9] is not related to a gradient in the oxygen vacancy concentration. This is an important finding because the sharp component has only been found in the crystallographically rather perfect samples with relatively high concentrations of oxygen vacancies and not in the less perfect Verneuil crystals with much lower oxygen vacancy concentrations. For a random distribution of these vacancies the mean distance of defects results to $d=n^{-1/3}$ with n representing the defect concentration. This distance varies between ≈240 Å for the lower defect concentrations and ≈40 Å for the higher concentrations (see Table II).

Special attention is devoted to sample I, where a direct correlation between strain, lattice parameter variation, and the occurrence of the sharp component in the critical scattering has been observed in the surface near region up to a

TABLE II. Bulk critical temperatures T_c and defect concentrations n of the different samples. $d=n^{-1/3}$ is the mean distance of defects, τ_d is the reduced temperature taken from the measurements of the inverse correlation length $[\kappa(\tau_d)=d^{-1}]$.

Sample no.		T_c (K)	n (cm^{-3})	d (Å)	$\frac{1}{d}$ (10^{-3} Å^{-1})	τ_d
I	Float-zone grown	98.8(1)	$6.1(2)\times10^{18}$	55(1)	18.2(2)	~0.115
II	Flux grown Verneuil grown	102.6(2)	$2.8(2)\times10^{18}$	71(2)	14.2(3)	~0.035
III	Oxidized	105.7(1)	$7.4(2)\times10^{16}$	238(2)	4.2(1)	~0.014
IV	As grown	105.8(1)	$7.6(2)\times10^{16}$	236(2)	4.2(1)	~0.025
V	Reduced	101.0(1)	$1.7(1)\times10^{19}$	39(1)	25.7(5)	~0.20

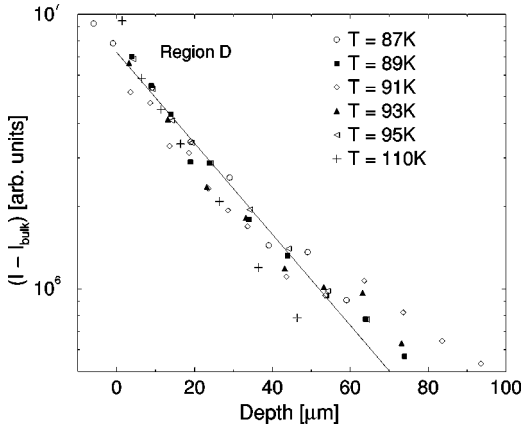

FIG. 3. Semilogarithmic plot of the depth dependence of the integrated intensity I of the (511) reflection in region D of sample I for different temperatures around the critical temperature with respect to the corresponding bulk value I_{bulk}. The increase of the integrated intensity in the surface near region is well described by an exponential relation with a $1/e$ length of $\zeta = 26(1)$ μm.

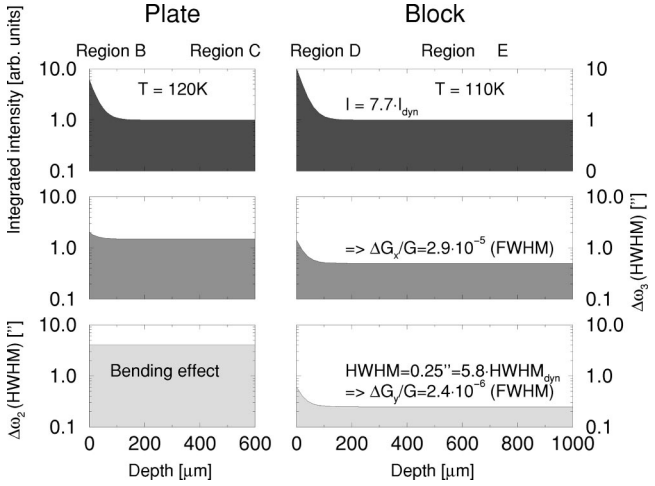

FIG. 4. Schematic view of the depth dependence of the integrated intensity and the half widths (HWHM) of longitudinal and transverse scans through the (511) Bragg reflection at $T = 110$ K and $T = 120$ K in sample I, respectively. The surface of the residual block (D) and the old surface of the plate (B) exhibit similar features, whereas the new surface of the plate (C) shows no difference from the bulk with respect to its crystallographic parameters. The intrinsic mosaicity of the plate (picture in the lower left corner) could not be measured due to the bending of the plate, shown in Fig. 6. The decay of all the crystallographic parameters at the different surfaces is well described by exponential functions with the same $1/e$ length of $\zeta \approx 25.5(15)$ μm.

depth of 100 μm, also using triple-crystal diffractometry at energies of ~ 120 keV.[9] Based on these results a 560 μm thick slice has been cut from the same sample. Figure 2 shows a schematical drawing of the sample before and after cutting. On the left-hand side the original sample is plotted. The capital letter A marks the region investigated in Ref. 9. The rectangular spots visualize the beam cross sections on the sample, however, the dimensions are not to scale. The cut was performed parallel to the surface at a depth of about 1 mm, using a diamond saw. The residual plate has a thickness of ~ 560 μm, the material loss due to sawing and careful polishing of the two cut faces resulted to about 1 mm. In Fig. 2 also the notation for the later discussion is defined. Region B is the surface near region of the upper surface of the cut plate, which has not been polished or treated otherwise. The region at the lower surface of the plate is labeled C. This surface corresponds to a depth of 560 μm with respect to the original sample surface. The region on top of the residual block is labeled D, this part of the crystal was at a depth of ~ 1.5 mm from the surface of the original block, i.e., it corresponds to the bulk of the original sample where no sharp component was observed. The two surfaces C and D had been subject to identical polishing treatment. Region E represents the bulk of the block. The depth dependent impedance measurements described above have been performed in region A, i.e., at the original sample.

In order to characterize the degree of perfection in sample I the depth dependence of the integrated Bragg-peak intensity, the mosaicity, and the variation of the lattice parameter have been measured at the (511) main reflection for the different surfaces B–D and in the bulk E of sample I (at temperatures close the phase transition temperature of ~ 100 K). In Fig. 3 the gain in the integrated intensity of the (511) Bragg reflection in region D with respect to the intensity I_{bulk} in the bulk (region E) is plotted as a function of the distance from the surface of the residual block. The straight line represents an exponential function $(I - I_{bulk}) \propto \exp(-z/\zeta)$ fitted to the data. No significant temperature dependence could be observed, the mean $1/e$ length is equal to $\zeta = 26(1)$ μm. The increase of intensity can be understood qualitatively on the basis of dynamical diffraction theory.[22,23] The bulk mosaicity of the sample is determined by transverse scans in reciprocal space, it results to a half width at half maximum (HWHM) of $\Delta\omega_2 = 0.25$ arcsec The width of the (511) reflection of an absolutely perfect $SrTiO_3$ crystal at 100 keV is $\mathrm{HWHM}_{dyn} = 0.043$ arcsec, i.e., the mosaicity is about a factor of 6 larger than the dynamical half width. This broadening is not an effect of the instrumental resolution but represents the intrinsic mosaic spread of the sample, which is still much smaller than in the other samples, especially the Verneuil-grown crystals showing mosaic spreads of 30–100 arcsec The integrated reflectivity I_{dyn} in the bulk expected for a perfect crystal is $I_{dyn} = 3.2 \times 10^{-7}$, neglecting absorption. In the bulk (region E) the measured integrated reflectivity after correction for absorption was about 7.7 times larger than the theoretical value I_{dyn}. This corresponds well to the increase in the mosaic spread. However, using the kinematical scattering theory, the expected integrated reflectivity of the 12 mm thick sample should be $I_{kin} = 7.0 \times 10^{-5} \approx 220 I_{dyn}$. Thus the diffraction mechanism in the bulk of this sample is close to the expectations for a perfect crystal, which has been shown before by means of diffraction experiments with 412 keV γ radiation.[24] Close to the surface the mosaic spread of the sample increases (Fig. 4), and therefore the scattering process has to be described more and more by kinematical scattering theory, which explains the increase of the integrated reflectivity, shown in Fig. 3. The HWHM of the transverse scans $(\Delta\omega_2)$, related to the mosa-

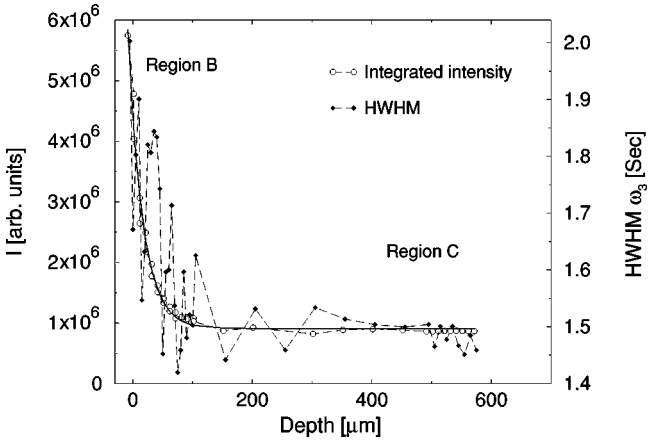

FIG. 5. Depth dependence of the integrated intensity I and the HWHM of the longitudinal scans at the (511)-reflection position in the $SrTiO_3$plate at $T=120$ K (sample I). The left-hand side corresponds to region B, the right-hand side to region C. The width of the longitudinal scans is proportional to the lattice parameter variations: $\Delta d/d=\frac{1}{2}\cot\theta_B\Delta\omega_3$. In region B, an exponential increase $\propto\exp(-z\zeta)$ of the integrated intensity and the lattice parameter variations is clearly visible. The $1/e$ length is equal to $\zeta=25(1)$ μm. The origin of the strong fluctuations in the measured lattice parameter fluctuations in region B is not clear, considering the data taken in region C as reference an experimental instability can be excluded. In region C no depth dependence is observed at all.

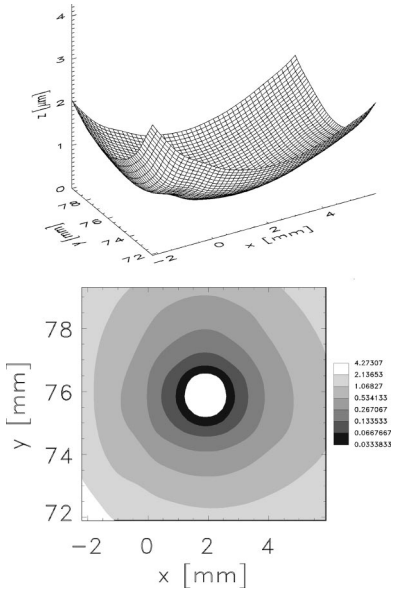

FIG. 6. Illustration of the bent plate in real space (sample I). The bending radius is about 14 m. Assuming the bent platelet as a segment of a sphere, then region B is outside and region C is inside the sphere.

icity, and the HWHM of the longitudinal scans ($\Delta\omega_3$), corresponding to the variation of the lattice parameter ($\Delta d/d=\frac{1}{2}\cot\theta_B\Delta\omega_3$, θ_B is the Bragg angle) follow the same exponential depth dependence as the integrated intensity shown in Fig. 3, the results are plotted in Fig. 4.

Figure 5 shows the variation of the integrated intensity together with the variation of the half width (HWHM) of the longitudinal scans, i.e., the lattice parameter variation across the platelet from surface B to surface C. On the left-hand side of the figure, which corresponds to region B, the behavior is identical to that in region D, shown in Fig. 3. Within the error bars, the $1/e$ length [$\zeta=25(1)$ μm] is the same. But, surprisingly, the other surface of the plate (region C) does not show any effect, neither for the integrated intensity, nor for the widths of the longitudinal scans. In fact, the integrated reflectivity is identical to the bulk value in region E, whereas the variation of the lattice parameter, $\Delta d/d$ is slightly enhanced compared to the bulk value. These results are also summarized schematically in Fig. 4.

The intrinsic mosaicity of the platelet could not be determined by these measurements because the platelet turned out to be bent. The secondary effects due to bending dominate the width of the diffraction pattern. An accurate determination of the bending radius was achieved by using a beam of narrow cross section, e.g., 50×50 μm^2, and measuring the shift of the position of a main reflection depending on the position in real space on the plate, which was oriented perpendicular to the incident beam. Using this technique, the curvature of the lattice planes can be reconstructed from the data (Fig. 6). The bending of the lattice planes is almost spherical, the bending radius is equal to ~14 m. In this figure, region C corresponds to the concave and region B to the convex side of the bent platelet. Using an optical microscope it could be seen that not only the lattice planes are bent but the platelet itself is bent macroscopically. It should be mentioned that the bending has been observed not directly after the polishing process but after the first low-temperature measurements, i.e., after the platelet had undergone the structural phase transition. Thus it is not clear if the bending process took place directly after the polishing process or some weeks later after cooling through the transition.

In addition to the depth dependent measurements with 100 keV photons, the surfaces B–D have been investigated in Bragg geometry with a photon energy of 20 keV on a triple-axis diffractometer at the HASYLAB beamline D4.[25] The absorption length at this energy was determined to $\mu^{-1}\sim55$ μm, i.e., the relevant contribution to the Bragg peaks results from the surface near region of some 10 μm thickness. In Fig. 7 the scattering profiles of the (200) Bragg reflection measured at the three surfaces B,C, and D are shown both in linear scale and in logarithmic scale (inset). At the surface of the residual block (region D) a difference between the center of the surface and the edge region of the surface was found. It can be seen that regions B and D (center) show much broader Bragg peaks than region C and the edge of the residual block (D edge). Additionally, the integrated intensity of the respective scans is shown in an inset. Consistent with the observations described above, the values are increased at surfaces B ($I=427$) and D ($I=321$), compared to surface C ($I=210$). For completeness it is interesting to note that at the edge of region D a behavior similar to the observations made in region C of the cut plate is found.

The characterization of the crystallographic quantities in sample I can be summarized as follows. The residual float-zone grown block consists of an almost perfect bulk (region E) covered by a layer (region D) of increased mosaicity and

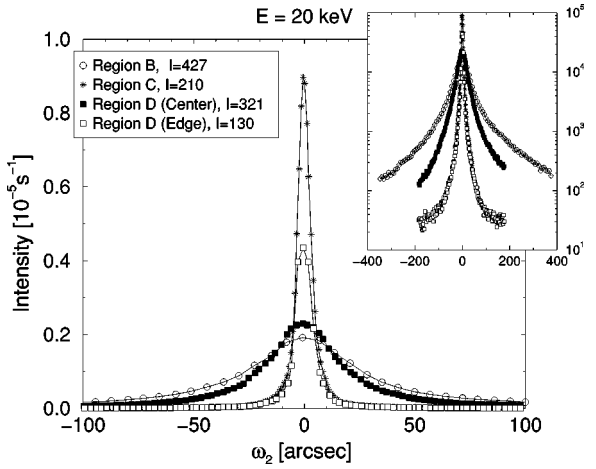

FIG. 7. Rocking curves of the (200) Bragg reflection measured at the different surfaces of the float-zone grown samples at room temperature with 20 keV x rays at HASYLAB beamline D4. The rocking curves in region B and in the center of region D of the residual block are much broader than those of region C and of the edge of region D. The inset on the right shows the same data on a logarithmic scale. *I* in the inset on the left-hand side represents the values of the integrated intensities of the respective rocking curves.

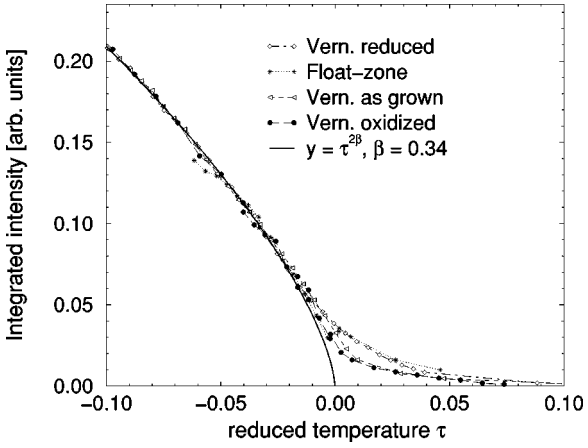

FIG. 8. Integrated intensities of the superlattice reflection (511)/2 measured in the bulk of sample I and of reflection (531)/2 measured in the bulk of samples III–V. In order to compare the tails above T_c the intensities have been normalized to their extrapolated value at $T=0$ K. The value of the critical exponent β has been fixed to $\beta=0.34$.

increased lattice parameter variations. Both mosaicity and lattice parameter variation increase exponentially with an $1/e$ length of $\cong 26(1)$ μm approaching the surface. This behavior is identical to the depth dependence of the experimental data from the original sample before the cut (region A), presented in Ref. 9, and supports the interpretations of the earlier γ-ray diffraction experiments on the same sample in Ref. 24. However, region D close to the surface of the residual block, which has been inside the almost perfect bulk of the sample before the cut, strongly changed its crystallographic properties after cutting and polishing the surface. On the other hand, the cut surface of the residual plate, i.e., region C shows no depth dependent effects neither in the lattice parameter variation nor in the integrated reflectivity. The values correspond well to those of the bulk (region E), only a slightly enhanced value of the lattice parameter variation is observed. In spite of the identical treatment of surfaces C and D, large differences are observed. The behavior of the untreated surface of the plate, region B, remains unchanged compared to the earlier measurements (region A).

The observed difference in the behavior of regions C and D can only be due to the fact that the plate became bent after the cut. Assuming that the original sample was affected by long-range strain fields in the bulk, possibly introduced by the growth process, a relaxation of these strain fields is not possible in the residual block because of its dimensions and the high degree of crystallographic perfection. In region D, close to the surface of the residual block, these strain fields lead to an increased mosaicity and to increased lattice parameter variations in the center of the surface, but not in the edge regions because here the strain fields may be able to relax. Similarly the relaxation of strain fields is observed in the platelet. The existing strain gradient in the platelet, experimentally determined at region A in Ref. 9, can relax by bending the whole thin sample. Hence, in region C the remaining strain field is weak and does not cause a detoriation of the crystal perfection. However, the other surface, region B, most probably still contains intrinsic defects due to surface damage because it was not polished and thus does not change its general behavior. Due to the large dimensions of the residual crystal block, such bending process is of course not possible at the sample surface, i.e., in region D.

Similar measurements have been carried out on sample II and a behavior very similar to that observed in regions A, B, and D of sample I was found at its surface. The mosaicity of sample II is about one order of magnitude larger than that of sample I, but it is still much better than the mosaic spreads of 30–100 arcsec of the Verneuil-grown crystals. The depth dependence of the crystallographic parameters of the Verneuil-grown crystals has not been investigated.

IV. CRITICAL TEMPERATURES

In order to determine the critical temperature T_c the temperature dependence of the integrated intensity of the superstructure reflections has been measured at (511)/2 in the bulk of samples I and II and at (531)/2 in the bulk of samples III–V. The data have been normalized to their extrapolated value at $T=0$ K and were plotted as a function of the reduced temperature $\tau=T/T_c-1$. The result is shown in Fig. 8. The tail observed above T_c depends on the defect concentration. It can originate from both the critical fluctuations and an additional contribution due to defects. However, for the determination of the critical temperature the effect of the defects has been neglected. Using the Landau approximation, the susceptibilitiy at $T_c-\Delta T$ is a factor of 2 smaller than the susceptibility at $T_c+\Delta T$ [see, e.g., Ref. 26]. This relation is used to subtract the contribution of the fluctuations below T_c as described in Ref. 6. The temperature dependence of the residual data I' can be fitted with the power law

$$I' \propto \left(\frac{T-T_c}{T_c}\right)^{2\beta}. \tag{1}$$

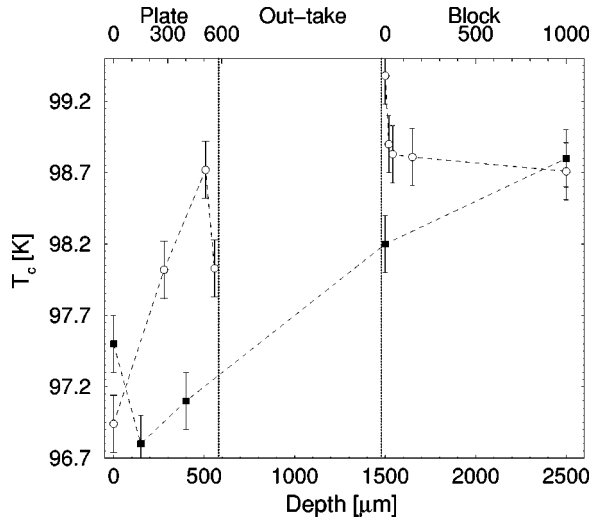

FIG. 9. Depth dependence of the critical temperatures in sample I after the cut (opaque circles), compared to the values for the original sample (black squares).

Applying this procedure leads to a shift in T_c of ~ 0.2 K to lower temperatures compared to completely ignoring the contribution of the tail. For a meaningful comparison of the critical temperatures T_c determined experimentally at different samples, the critical exponent β was fixed to $\beta = 0.34$. Slight changes in β were allowed to determine the error bars of the critical temperatures. The results for the critical temperature in the bulk of the various samples are summarized in Table II. The value $T_c = 98.8(1)$ K for sample I has been determined in the bulk of the original sample. The values of the critical temperature quoted in the literature accumulate at about 105 K. This value is similar to those found in the present study for the two Verneuil crystals (samples III and IV) with low oxygen vacancy concentrations (see Table II). It has been shown earlier that an increased amount of oxygen vacancies reduces the critical temperature,[27,28] the value of T_c determined at the reduced Verneuil sample nicely reproduces these results. However, the shift in the critical temperature for the two highly perfect samples I and II is much too large with respect to the experimentally determined concentration of oxygen vacancies. The origin of this observation is not clear yet, perhaps the high degree of perfection of samples I and II has an effect on the low transition temperature. As pointed out by Zhong *et al.*,[29] the existence of quantum fluctuations can lead to a significant decrease of the critical temperature by up to 20 K. It might be speculated that quantum fluctuations show a stronger effect in the highly perfect samples than in the worse Verneuil crystals and could thus contribute significantly to the decrease of T_c.

In analogy to the crystallographic characterizations described above, the depth dependence of the critical temperature has been investigated in detail in sample I. The results are plotted in Fig. 9. Both the transition temperatures before and after the cut are shown. As to be expected no changes in T_c are observed in region E, the bulk of the sample. In the original sample two features can be identified. Over a large range the critical temperature is decreasing and close to the surface, in region A, a slightly enhanced value for T_c is found. The latter observation is similar to the behavior at the surface of the residual block, region D. There one also finds a slight increase in the critical temperature very close to the surface (~ 20 μm). However, in the thin plate a different behavior is observed. 50 μm below the surface of region C of the cut plate, T_c is identical to the bulk value (region E), but at the surfaces, regions B and C, the critical temperature is decreased substantially. Comparing these observations with the results of the crystallographic characterization, it can be concluded that two different effects have to be distinguished. On the one hand, the probably large amount of dislocations and other defects due to surface damage in region A, which are not yet identified, could be responsible for the large difference in the transition temperatures found in the bulk and near the surface of the original block. On the other hand, it seems that the strain fields in its surface near region increase the transition temperatures slightly. This is observed in region A and region D, but not in region C, where the strain fields are absent and the critical temperature reaches a value close to the bulk value (region E). At the surface of region B, however, the value of T_c is strongly reduced.

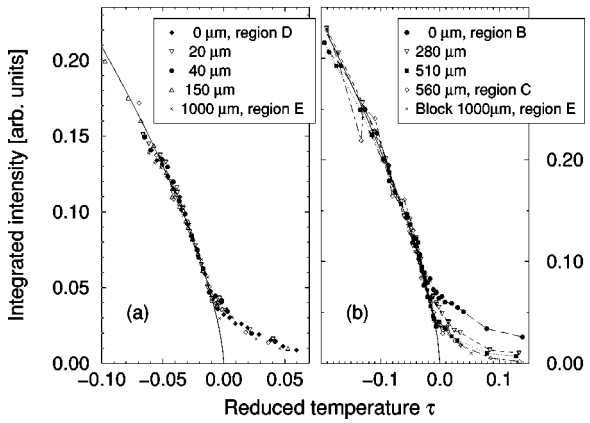

FIG. 10. Temperature dependence of the integrated intensities of the (511)/2 superlattice reflection, normalized to the respective extrapolated value at zero temperature, for different positions (a) in the residual block and (b) in the plate of sample I. The tail above T_c is almost independent of the distance from the surface. Only in region B significant changes in the temperature dependence of the tail are observed.

Another interesting result of the measurements is the behavior of the tails of the squared order parameter above the critical temperatures. In order to compare the tails for the different samples, the integrated intensities of the superlattice reflection have again been normalized to the respective scaling factor of the fitted power law, i.e., the extrapolated value at zero temperature and plotted as a function of the reduced temperature τ. This way, the effect of the stronger, more kinematical scattering at the surface is canceled out and all curves except one coincide above the transition temperature, as can be seen in Fig. 10. The additional information derived from this kind of presentation is the similarity of the temperature dependence of the tails above the critical temperatures. In the residual block [Fig. 10(a)], all data points follow the same trend above T_c, i.e., the nature of the tails is not connected to the observed strain gradients at the surface.

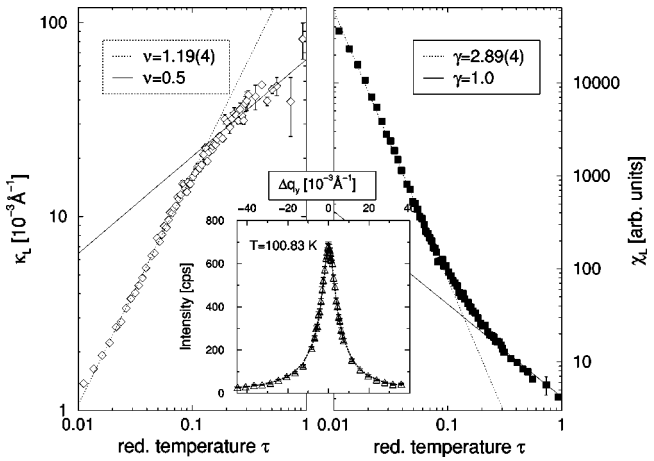

FIG. 11. Temperature dependence of inverse correlation length and susceptibility of the broad component in the bulk of the float-zone grown sample (I), measured at the position of the (511)/2 superlattice reflection. Around $\tau_{cr}=0.11$ a crossover in the critical behavior is clearly visible. The inset shows a transverse scan (Δq_y) and the best fit to the data at $T=100.8$ K.

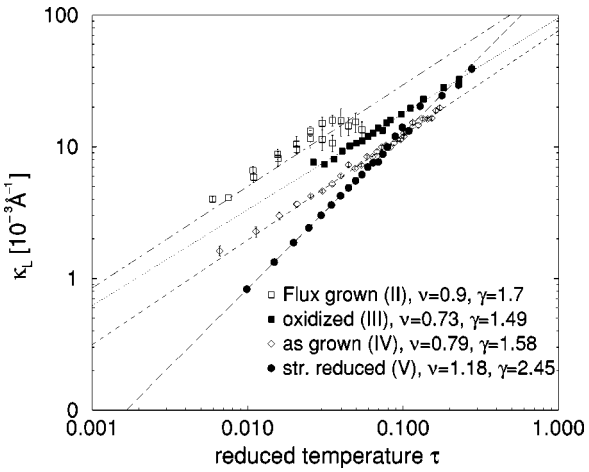

FIG. 12. Inverse bulk correlation length for samples II to V. The effective exponents ν_b and γ_b have been derived from power-law fits to the inverse correlation length and the susceptibility not shown in the figure.

Moreover, the tails are identical in the residual block and in the thin plate [Fig. 10(b)], only the old surface of the plate, region B, shows a significantly enhanced amount of scattering above T_c. Certainly, this has to be attributed to the larger amount of dislocations and/or other defects in this region due to surface damage.

V. CRITICAL SCATTERING IN THE BULK—THE BROAD COMPONENT

The temperature dependence of the critical scattering has been measured in the bulk of samples I and II at the superlattice reflection (511)/2, as well as in the bulk of the three Verneuil-grown crystals [reflection (531)/2]. After deconvolution from the experimental resolution function the scattering profiles could be fitted with a single Lorentzian distribution function, which is called the broad component in contrast to a much narrower component found in the surface near region of some of the crystals investigated. From the half width-half maximum and the peak of these single Lorentzians the inverse correlation length κ_b and the susceptibility χ_b have been determined. The corresponding critical exponents ν_b and γ_b were determined by fitting the experimental data to the power laws

$$\kappa_b(\tau)\propto\tau^{\nu_b} \quad \text{and} \quad \chi_b(\tau)\propto\tau^{-\gamma_b}. \tag{2}$$

The critical scattering in the float-zone grown sample has been measured over a much larger temperature interval than those of the other samples. Here, a crossover between different values for the critical exponents ν_b and γ_b obtained from $\kappa_b(\tau)$ and $\chi_b(\tau)$ can be identified (see Fig. 11). These data have been taken in the bulk of the sample but the probed volume also included two surfaces (the front and the back side). However, due to the relatively large thickness (12 mm) of the sample, the possible contribution of a sharp component to the critical scattering, originating from a thin layer at the surface, was estimated to less than 1% close to T_c and has been neglected.

Around the crossover temperature τ_{cr} a change of slope is clearly visible for both $\kappa_b(\tau)$ and $\chi_b(\tau)$. This crossover temperature τ_{cr} is in excellent agreement with the value of τ_d (see Table II) defined as following: τ_d is the reduced temperature at which the correlation length $\kappa_b^{-1}(\tau_d)$ is equal to the mean distance d of the oxygen vacancies. Above this crossover temperature $\tau_c=\tau_d$ the system can be described within mean-field theory, which leads to the exponents $\nu_b=0.5$ and $\gamma_b=1.0$, below the crossover temperature the exponents $\nu_b=1.19(4)$ and $\gamma_b=2.89(4)$ are determined by the fit. The nonclassical exponents expected for this three-dimensional Heisenberg system with cubic symmetry, calculated by LeGuillou and Zinn-Justin,[30] are much lower: $\nu=0.705(3)$ and $\gamma=1.386(4)$. On the other hand the ratio $\chi_b/\nu_b=2.2(2)$ is in good agreement with the theoretical value of $\chi/\nu=1.97$.[30]

In Fig. 12 the inverse correlation length for the four other samples is plotted against the reduced temperature. Effective exponents ν_b and γ_b have been derived by fits of power laws to each data set without taking into account the crossover scenario, because the expected crossover temperature τ_d is either too small (≈ 0.02) or too large (0.20) to allow an observation of the crossover within the probed temperature range. As shown in Table III the effective exponents vary between $\nu\approx 0.75$, $\gamma\approx 1.5$ (as grown and oxidized Verneuil-grown samples) and $\nu\approx 1.2$, $\gamma\approx 2.4$ (reduced Verneuil-grown sample). It should be emphasized that the scaling relation $\gamma=(2-\eta)\nu$, with $\eta\approx 0.03$,[31] still holds.

VI. CRITICAL SCATTERING NEAR THE SURFACE—THE SHARP COMPONENT

In the surface near regions of the crystallographically highly perfect samples I and II a pronounced sharp component has been observed in the critical scattering measured at

TABLE III. Critical exponents ν_b and γ_b for the broad component.

Sample no.	Broad component ν_b	γ_b	γ_b/ν_b
Original block			
I, region A	1.02(4)	2.32(7)	2.27 (11)
Residual plate			
I, region B	1.19	2.23(10)	1.87(11)
I, region C	1.19	2.83(10)	2.38(13)
Residual block			
I, region D	1.19	2.53(3)	2.13(9)
I, region E	1.19(4)	2.89(4)	2.43(9)
II	0.9(1)	1.7(1)	1.9(2)
III	0.73(7)	1.49(15)	2.04(28)
IV	0.79(2)	1.58(7)	2.00(10)
V	1.18(3)	2.45(7)	2.08(8)

temperatures above T_c at the position of the (511)/2 superstructure reflection in addition to the broad component discussed above. As described in the Appendix the scattering profile could be fitted with the sum of a single Lorentzian and a Lorentzian-squared profile, i.e., two additional parameters, the inverse correlation length κ_s and the susceptibility χ_s have to be taken into account. The peak position of the two contributions turned out to be identical. A typical example of a measured scattering profile is shown in Fig. 13. The Lorentzian-squared part is much narrower than the Lorentzian shaped contribution, which is the reason for calling it the sharp component.

The depth dependence of the critical scattering profile as measured at a temperature about one degree above T_c in the surface near region of the residual block of sample I is shown in Fig. 14. In the top 20 μ m, region D, the additional sharp component is clearly visible. In the inset, the same data are plotted on a logarithmic scale over a wider angular range.

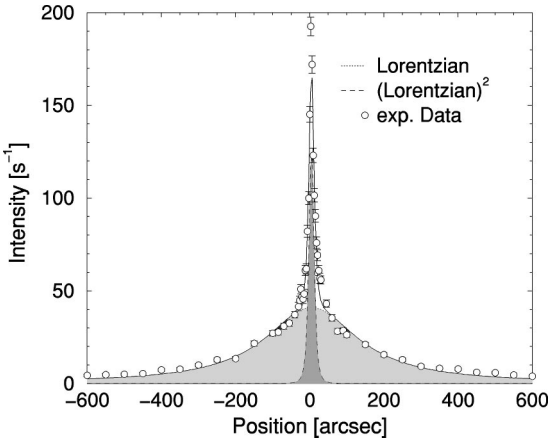

FIG. 13. Transverse scan through superlattice reflection (511)/2 at sample I measured 0.5 K above T_c in a distance of 20 μm from the surface of the residual block (region D). In addition to the broad Lorentzian distribution a sharp Lorentzian-squared profile is visible at the position of the superlattice reflection.

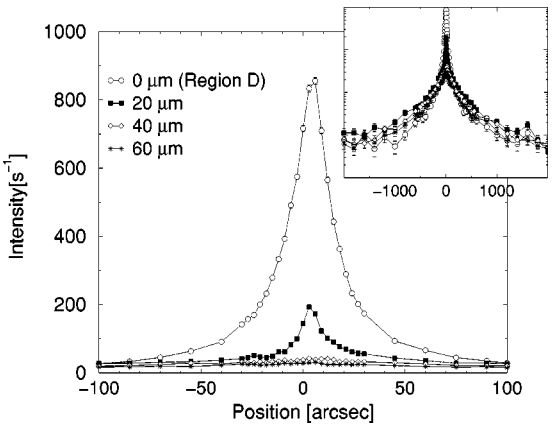

FIG. 14. Transverse scan profile of the (511)/2 superlattice reflection about 1 K above the critical temperature for different distances to the surface of the residual float-zone grown block (sample I, region D). For the top 20 μm the intensity is strongly enhanced in a narrow region around the superlattice position. The inset shows the measured data over a much larger angular range in a logarithmic scale. It can be seen that all profiles are almost identical if the sharp component is not considered.

This is to stress the observation that the broad component is independent of the location of the probed volume element in the sample. The scattering differs only in the central region, where the sharp component dominates. The temperature dependence of the inverse correlation length for the broad component measured in the surface near region was identical at all investigated positions in sample I after the cut, i.e., the occurrence of the sharp component as well as the increased mosaicity and lattice parameter variations do not affect the behavior of the broad component. The values ν_b and γ_b for the critical exponents of the broad component in the different samples and for the various positions in the samples are summarized in Table III. In Table III also the validity of the scaling relation

$$\gamma = (2-\eta)\,\nu \approx 2\,\nu \tag{3}$$

is checked. For all measurements the ratio χ_b/χ_b for the broad component is close to 2 and fulfills scaling relation (3) very well because η is very small.

Figure 15 shows a direct comparison of the critical scattering measured at surface regions B, C, and D in the float-zone grown sample I. Apparently, the width of the sharp component in region B is much broader than the respective width in region D. Furthermore, almost no signal of the sharp component is visible in region C. The profiles for regions C and D are identical except for the narrow region in the center of the scan, where the sharp component occurs. At this point it is interesting to note that in the case of the float-zone crystal the sharp component measured with 100 keV synchrotron radiation at a superlattice reflection with scattering vector parallel to the crystal surface is about one order of magnitude narrower than the sharp component measured by Hirota *et al.*[13] with 11.5 keV x rays at a reflection with scattering vector perpendicular to the surface.

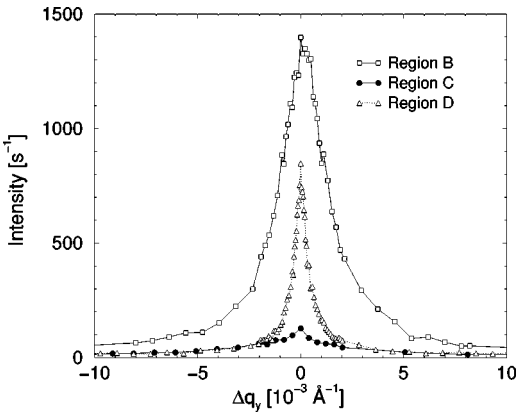

FIG. 15. Comparison of the scattering profiles of the (511)/2 superlattice reflections of sample I 1 K above T_c measured close to the three different surfaces. The old surface of the plate (region B) differs strongly from the other ones, whereas the new surface of the plate (region C) and the residual block (region D) differ only in the narrow region in the center of the plot. The broad component of the critical scattering is identical for the latter two surfaces, but at the residual block the sharp component can be observed in addition.

In Fig. 16 the plots from which the critical exponents γ_s [Fig. 16(a)] and ν_s [Fig. 16(b)] have been determined are shown for the four surface near regions in sample I and II where the sharp component was observed. Again, the old surface of the cut-off plate, region B, strongly differs from all other data sets. Here we expect a gradient in a rather high density of defects caused by surface damage in the otherwise strain relaxed bent crystal plate. The resulting values for the critical exponents of the sharp component are listed in Table IV. Interestingly, the ratio γ_s/ν_s is noticeable larger than 2, more likely close to 4.

The validity of scaling relations for the sharp component could be preserved, if the intensity of the sharp component is

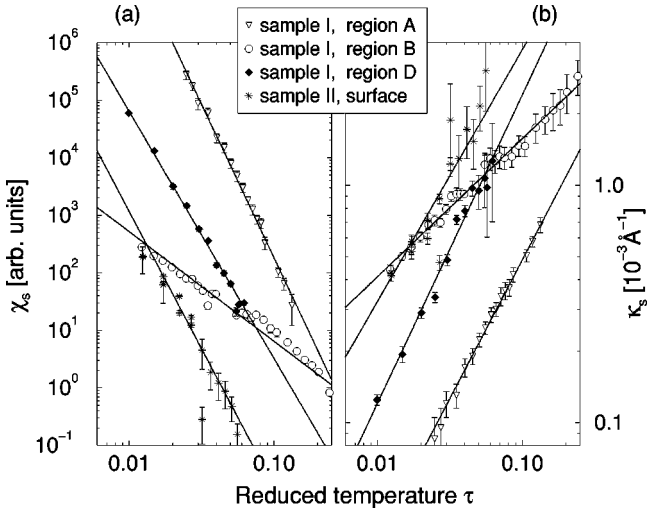

FIG. 16. Temperature dependence (a) of the inverse correlation length κ_s and (b) of the susceptibility χ_s of the sharp component for the different surfaces. The critical exponents ν_s and γ_s are similar for most of the investigated surfaces, but they strongly deviate at the old surface of the plate (region B).

TABLE IV. Critical exponents ν_s and γ_s as well as the ratio γ_s/ν_s for the sharp component. The ratio γ_s/ν_s is more likely close to 4 than to the expected value of 2.

	Sharp component		
Sample no.	ν_s	γ_s	γ_s/ν_s
I, region A	1.17(4)	5.33(9)	4.6(2)
I, region B	0.58(5)	1.9(2)	3.3(4)
I, region D	1.30(5)	4.29(10)	3.30(14)
II, surface	1.1(1)	4.8(1)	4.4(4)

not proportional to the susceptibility but to the square of the susceptibility. The two functions

$$I_s = \frac{\chi_s}{\left[1+\left(\frac{\mathbf{q}}{\kappa_s}\right)^2\right]^2} = \hat{\chi}_s(\mathbf{q},T) \tag{4}$$

and

$$I_s = \left(\frac{\chi_s'}{1+\left(\frac{\mathbf{q}}{\kappa_s}\right)^2}\right)^2 = \hat{\chi}_{Ls}'^2(\mathbf{q},T) \tag{5}$$

only differ by the definition of the respective susceptibility. All critical exponents discussed so far have been derived using Eq. (4). However, assuming a Lorentzian distribution and using the latter definition, the susceptibility χ_s is replaced by $\chi_s' = \sqrt{\chi_s}$. As a result, the value of the critical exponent is reduced by a factor of two, $\gamma_s' = \gamma_s/2$ and the ratio γ_s'/ν_s is close to two, fulfilling the scaling relation (3). At present, we do not have a physical justification for this formal appproach to describe the sharp component.

The different theoretical approaches to explain the two length scale problem were summarized by Cowley.[1] In agreement with the present results there is a consensus that the phenomena is a surface related effect and that strain, which could be highly anisotropic in a near surface layer, plays an important role. Altarelli *et al.*[32] and Harris *et al.*[33] consider explicitly certain forms of disorder and strain in the skin layer. Altarelli *et al.*[32] assume that high densities of defects with long range interactions in the near surface region modify the critical behavior and depending on whether point, line, or planar defects dominate they suggest values of 2, 1, or 1/3 for the critical exponent ν_s. The value of $\nu_s = 1$ corresponding to dislocations is in good agreement with the experimental data, however, the suggested value of $\chi_s/\nu_s = 2$ for the ratio of the critical exponent is in clear disagreement with the experimental value of $\chi_s/\nu_s = 4.4$ if the Lorentzian-squared distribution of Eq. (5) is used to describe the sharp component of the critical scattering. Harris *et al.*[33] emphasize the random field effects of near-surface defects and dislocations. The Lorentzian-squared component is expected to be due to symmetry breaking or random field producing defects. The critical exponents ν for the correlation lengths for both length scales should be about the same $\nu_b \approx \nu_s$, which is in fair argument with the experimental data

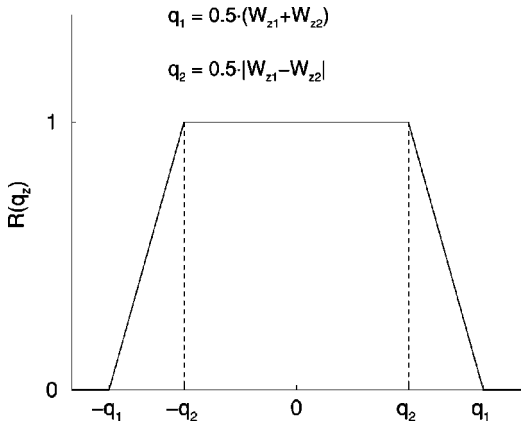

FIG. 17. Resolution function perpendicular to the scattering plane. The horizontal part of the trapezoid has a width of $2q_2 = |W_{z1} - W_{z2}|$, the width of the sloped parts just corresponds to the width of the smaller slit. In the case $W_{z1} \ll W_{z2}$ the trapezoid degenerates to a rectangle.

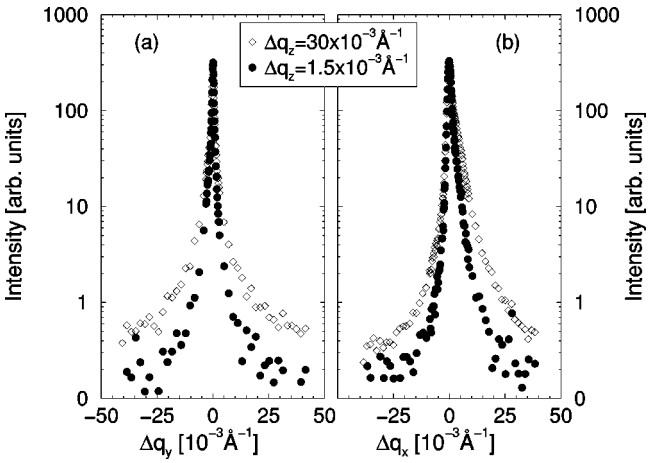

FIG. 18. Suppression of the broad component due to improvement of the resolution vertical to the scattering plane shown for transverse (a) and longitudinal (b) scans. Filled circles refer to scans with Δq_z 1.5×10^{-3} Å^{-1}, open diamonds represent scans with $\Delta q_z = 30\times10^{-3}$ Å^{-1}.

obtained at the samples I and II, except region B of sample I. Assuming a random field[34] the ratio γ_s/ν_s is then twice the value of γ_b/ν_b, which is also in agreement with the experimental value.

VII. DISCUSSION

In order to study the effect of defects on the critical behavior at the cubic-tetragonal structural phase transition in $SrTiO_3$, the critical scattering at superlattice reflections (511)/2 and (531)/2, respectively, has been measured in five different samples of different degree of crystallographic perfection and different concentration of oxygen vacancies. Special attendance has been payed to the difference in the critical behavior in the bulk and in the surface near region of the samples.

The long-range crystallographic perfection has been discussed on the basis of the results from high-resolution Bragg-scattering experiments using highly penetrating 100 keV synchrotron radiation. It turns out that the float zone as well as the flux grown samples are almost perfect crystals, whereas the three Verneuil crystals show a much broader diffraction pattern and are expected to have a rather high dislocation density. In a surface near region of about 100 μm thickness of the two highly perfect crystals a gradient in the strain, i.e., in the lattice parameter fluctuations, the mosaicity and the integrated Bragg peak reflectivity is observed, which is related to the occurrence of the sharp component of the critical scattering. In order to prepare a defect free surface at the large float-zone grown crystal a 0.57 mm thick platelet was cut off from the sample, both the new surface of the platelet and that of the remaining crystal block have been carefully polished and etched. In the surface near region of the remaining crystal block again a gradient in the lattice parameter fluctuations, the mosaicity and the integrated Bragg peak intensity has been observed. The cut-off platelet turned out to be spherically bent and no gradient in the degree of crystal perfection was observed at the cut surface.

For the bulk of the samples the concentration of oxygen vacancies has been determined from conventional impedance measurements, in the case of very high concentration from Hall resistivity measurements. At the polished surface of the remaining float-zone grown crystal block as well as at the flux grown crystal a depth dependent determination of the oxygen vacancy concentration has been performed using a special type of impedance spectroscopy and no gradient was found. Therefore a homogeneous distribution of oxygen vacancies has been assumed for the discussion of the critical behavior.

Below T_c the temperature dependence of the superlattice reflections could be fitted with a power law with exponents β very close to the accepted literature value of 0.34. For reasons of comparison between the different samples and between their behavior in the bulk and in the surface near region the critical temperature has then been determined from fitting the temperature dependence of the superlattice reflection with a fixed value of $\beta = 0.34$. In agreement with earlier findings the critical temperature measured in the bulk of the samples decreases with increasing oxygen vacancy concentration. Furthermore, in the float-zone grown crystal T_c decreases by about 2 K over a thickness of 2.5 mm when approaching the surface from the bulk, this effect is assumed to be due to a long-range strain gradient. In a 100 μm thick surface layer the gradient changes sign and T_c increases by almost 1 K, this effect is assumed to be due to a more localized gradient in the dislocation density due to surface damage. A similar effect is observed in the surface near region of this crystal after cutting a 1 mm thick layer and carefully polishing the surface. In the cut-off platelet a strong variation of T_c is also observed, however, the gradient in the surface near region is of opposite sign.

In the less perfect Verneuil-grown crystals with significantly different oxygen vacancy concentrations the critical behavior has been studied by measuring the temperature dependence of the (531)/2 superlattice reflection. No sharp component was observed, neither in the bulk nor at the surface. For the as grown and the oxidized crystal the critical

exponents ν_b and χ_b of the broad component agree very well with the theoretical values obtained by LeGuillou and Zinn-Justin.[30] For the reduced crystal with a rather high oxygen vacancy concentration the values of these critical exponents are much higher, however, the ratio χ_b/ν_b is again very close to 2, as required by the scaling laws.

In the perfect flux and float-zone grown crystals a sharp component has been observed in the critical scattering in the surface near regions that showed a gradient in strain, mosaicity, and integrated Bragg peak intensity. The critical exponents of the broad component were very little affected by the occurrence of the sharp component. For the flux grown crystal the ratio χ_b/ν_b was equal to 2, for the float-zone grown crystal the values determined in the bulk and at the different surfaces scatter around an average value of $\chi_b/\nu_b = 2.2$.

The critical scattering above the cubic-to-tetragonal phase transition of $SrTiO_3$ was investigated in five different samples. The main focus was on the dependence of the critical phenomena on the distance of the probed volume element in the sample from its surface. In order to interpret the results concerning the critical scattering, the crystallographic perfection was analyzed with high momentum and high real-space resolution, especially in the regions close to the surfaces. Emphasis was on the differences between several surfaces of the highly perfect float-zone grown crystal (sample I).

As a result it is observed that one necessary condition for the existence of two length scales in the critical scattering is the vicinity (some 10 μm) of the sample surface. Another necessary condition is the existence of strain fields in this region, experimentally demonstrated by the increase of lattice parameter variations and mosaicity close to the surface. However, in samples of lower quality, i.e., with strongly enhanced mosaic spreads the sharp component is suppressed significantly compared to that found in the highly perfect crystals. Possibly the long-range order of the corresponding critical fluctuations is destroyed by the high amount of topological defects in samples of high mosaicity. It should be mentioned that, qualitatively, it has been shown in earlier work that a distorted surface can reduce the intensity of the sharp component.[7,10]

Starting with the bulk of sample I, region E, no sharp component could be observed, because it is not a surface near region. In region D, both conditions are fulfilled. Both mosaicity and the variation of the lattice parameter, as well as the critical temperature, increase exponentially approaching the surface due to the exisitence of long-range strain fields at this surface. Simultaneously, also the intensity of the sharp component increases, while the broad component remains unaffected. Region C consists of a locally almost perfect crystal, where the long-range strain fields were able to relax by bending of the lattice planes. Thus, no sharp component is observed and the critical temperature is close to the bulk value. Although the long-range strain could relax also in region B due to the bending of the plate, a strong sharp component is still observed. This could be due to a gradient in the density of dislocations and other unspecified defects expected in this region due to surface damage caused by the frequent use of this sample for many different experiments over more than 30 years. This way the conditions for the sharp component to occur are fulfilled, however, the strain gradient in the surface near region B is of different origin. The development of the long-range correlations leading to the sharp component in the other, almost defect free regions of the crystals, could be partly suppressed by the defects in region B. This would explain the differences observed in the measurements at the ''old'' surface before and after cutting off the plate, i.e., in regions A and B. It would also explain the differences between region B and all the other regions investigated with respect to the amount of critical scattering above T_c, the shape of the sharp component, and the critical exponents. The behavior of sample II at the surface is very similar to the behavior of sample I in region D. In the surface near region mosaicity, lattice parameter variation, and the intensity of the sharp component increased with respect to the bulk values. Compared to these two, almost perfect samples the intensity of the sharp component in the Verneuil-grown samples III–V is suppressed by about three orders of magnitude, i.e., no evaluation of critical exponents for this component was possible. Following the above reasoning this should be due to the large mosaicity corresponding to a very high density of defects, which suppresses the long-range correlation even more than in the old surface of the plate of sample I (region B).

In conclusion, long-range strain fields in the vicinity of the surface seem to be responsible for the second length scale in the critical scattering of $SrTiO_3$. These long-range strain fields can spread out much better in almost perfect crystals, dislocations and other topological defects weaken these strain fields, they affect the critical exponents and eventually lead to complete suppression of the second length scale. Similar to the usual critical fluctuations, the temperature dependence of the long-range correlations can be described with a set of critical exponents. However, the distribution of defects in the surface near region is crucial for the formation of the sharp component and for the values of the critical exponents describing this phenomenon. Comparison with theory[30–34] has been made. In addition, Cowley[1] suggested that at the crystal surface the coupling of strain fields to the order parameter might lead to free surface waves with a higher effective transition temperature than the bulk fluctuations. The sharp component is then attributed to the free surface fluctuations. Unfortunately, no quantitative calculations on the basis of this approach have been performed yet. Further theoretical work is needed for a full quantitative understanding of the nature of the second length scale in the critical scattering.

ACKNOWLEDGMENTS

We would like to thank H.J. Scheel for making available the flux-grown $SrTiO_3$ crystal, S. Kapphan for preparing the Verneuil crystals, and K.A. Müller and E. Courtens for stimulating remarks. Valuable comments from B. Kaufmann and F. Schwabl are gratefully acknowledged. The work was supported by U.S. Department of Energy under Contract No. DE-AC02-98CH10886.

APPENDIX: DECONVOLUTION OF THE RESOLUTION FUNCTION

In order to extract the correlation length and the susceptibility from the experimental data, first the experimental resolution function had to be determined. The deconvolution procedure is based on the paper by Hirota *et al.*[13] In the scattering plane, the resolution function was determined experimentally at the position of the superstructure reflection a few degrees below the transition temperature (see Fig. 1). From these scans the widths in the longitudinal (FWHM_x) and in transvere (FWHM_y) directions, and the shape of the respective scattering profiles were extracted. In most cases, the shape of the superstructure peak could be well described by means of a Lorentzian-squared profile. The functional form of the resolution element was approximated by

$$R(q_x,q_y)=\left[1+\left(\frac{q_x}{\sigma_x}\right)^2+\left(\frac{q_y}{\sigma_y}\right)^2\right]^{-2},$$

$$\sigma_{x,y}=\frac{\mathrm{FWHM}_{x,y}}{2\sqrt{\sqrt{2}-1}}. \tag{A1}$$

For the investigated samples this approximation is in very good agreement with the correct resolution function, the theoretical calculation is explained in detail in Refs. 35,36. Perpendicular to the scattering plane, the resolution is determined by the opening of the vertical slits, substantially by the widths of the slits in front of the sample (S_{z1}) and in front of the detector (S_{z2}). These widths have to be transformed to **q** space using the distance L between sample and detector and the value of the wave vector **k**:

$$W_{zi}=|\mathbf{k}|\frac{S_{zi}}{L}. \tag{A2}$$

The resolution element $R(q_z)$ is now given by the convolution of two rectangular profiles, which is a trapezoidal function, as shown in Fig. 17,

$$R(q_z)=\left\{\begin{array}{cc} 0 & \forall |q_z|\geqslant q_1 \\ \dfrac{|q_z|-q_1}{q_2-q_1} & \forall q_2<|q_z|<q_1 \\ 1 & \forall |q_z|\leqslant q_2 \end{array}\right\}, \tag{A3}$$

$$q_1=\frac{1}{2}(W_{z1}+W_{z2}),$$

$$q_2=\frac{1}{2}|W_{z1}-W_{z2}|. \tag{A4}$$

For an incident intensity I_0 the scattered intensity $I(\mathbf{q})$ results to

$$\frac{I(\mathbf{q})}{I_0}=\int\int\int dq_x'dq_y'dq_z'R(q_x',q_y')R(q_z')I_{crit}(\mathbf{q}-\mathbf{q}'), \tag{A5}$$

where I_{crit} is the intrinsic profile of the critical scattering, typically a Lorentzian distribution. As described above, in some cases the critical scattering cannot only be described by a single Lorentzian profile. We used an additional isotropic Lorentzian-squared function to fit the experimental data,

$$I_{crit}=I_{Lor}+I_{Lq}, \tag{A6}$$

$$I_{Lor}=\frac{\chi_{Lor}}{1+\sum_{i=x,y,z}\left(\dfrac{q_i-q_{i,0}}{\kappa_{Lor,i}}\right)^2}, \tag{A7}$$

$$I_{Lq}=\frac{\chi_{Lq}}{\left[1+\left(\dfrac{\mathbf{q}-\mathbf{q_0}}{\sigma_{Lq}}\right)^2\right]^2}. \tag{A8}$$

According to Ref. 4, the Lorentzian contribution shows an anisotropy, the inverse correlation lengths κ_{100} in (100) directions are by a factor of 1.8 smaller than κ_{011} in (011) directions. In the present experiments the scattering geometry was such that $q_x\|$ (511), $q_y\|$ ($\bar{1}50$), and $q_z\|$ ($\bar{5}\bar{1}26$), i.e., all three directions are slightly tilted with respect to the main axes. For simplicity we assumed $\kappa_x\approx\kappa_y\approx\kappa_z\approx\kappa_{100}\equiv\kappa_{Lor}$, probably slightly underestimating the correct inverse correlation length.

The integration in q_z in Eq. (A5) was performed analytically. Using the symmetry of the resolution function, the integral reduces to

$$\int dq_z'R(q_z')I_{crit}(\mathbf{q}-\mathbf{q}')$$
$$=2\int_0^{q_2}dq_z'I_{crit}(\mathbf{q}-\mathbf{q}')+2\int_{q_2}^{q_1}dq_z'\frac{q_z'-q_1}{q_2-q_1}I_{crit}(\mathbf{q}-\mathbf{q}'). \tag{A9}$$

The integral consists of four parts, two addends for both the Lorentzian I_{Lor}^{conv} and the Lorentzian-squared contribution I_{Lq}^{conv}. Now we define

$$b_L^2=\kappa_{Lor}^2+(q_x-q_x')^2+(q_y-q_y')^2, \tag{A10}$$

$$b_{Lq}^2=\sigma_{Lq}^2+(q_x-q_x')^2+(q_y-q_y')^2, \tag{A11}$$

and set $q_z=0$, because we are only looking at the intensity in the scattering plane. The result for the Lorentzian part can be written as

$$I_{Lor}^{conv}=\frac{\chi_{Lor}\kappa_{Lor}^2}{b_L}\left[2\arctan\left(\frac{q_2}{b_L}\right)+\frac{j_1-j_2}{q_2-q_1}\right], \tag{A12}$$

where

$$j_1=b_L\ln(b_L^2+q_1^2)-2q_1\arctan(q_1/b_L), \tag{A13}$$

$$j_2=b_L\ln(b_L^2+q_2^2)-2q_1\arctan(q_2/b_L). \tag{A14}$$

Equation (A12) can be simplified to

$$I_{Lor}^{conv} = \frac{\chi_{Lor}\kappa_{Lor}^2}{q_2 - q_1}\left[\ln\left(\frac{b_L^2+q_1^2}{b_L^2+q_2^2}\right) - 2\frac{q_1}{b_L}\arctan\left(\frac{q_1}{b_L}\right) + 2\frac{q_2}{b_L}\arctan\left(\frac{q_2}{b_L}\right)\right]. \quad \text{(A15)}$$

Similarly, the integration of the Lorentzian-squared part yields

$$I_{Lq}^{conv} = \frac{\chi_{Lq}\sigma_{Lq}^4}{b_{Lq}^3(b_{Lq}^2+q_2^2)}\left\{q_2 b_{Lq} + (q_2^2+b_{Lq}^2)\arctan\left(\frac{q_2}{b_{Lq}}\right) + b_{Lq}q_2^2 - q_1 b_{Lq} + q_1(b_{Lq}^2+q_2^2)\left[\arctan\left(\frac{q_1}{b_{Lq}}\right) - \arctan\left(\frac{q_2}{b_{Lq}}\right)\right]\right\}$$

$$\Leftrightarrow I_{Lq}^{conv} = \frac{\chi_{Lq}\sigma_{Lq}^4}{b_{Lq}^3(q_2-q_1)}\left[q_2\arctan\left(\frac{q_2}{b_{Lq}}\right) - q_1\arctan\left(\frac{q_1}{b_{Lq}}\right)\right]. \quad \text{(A16)}$$

The remaining calculations,

$$\frac{I(q_x,q_y)}{I_0} = \int\int dq_x' dq_y' R(q_x',q_y')(I_{Lor}^{conv} + I_{Lq}^{conv}), \quad \text{(A17)}$$

have been evaluated numerically, using the approximation (A1) for the resolution element in the scattering plane, and were compared to experimental data $I(q_x=0,q_y)$ for transverse scans or $I(q_x,q_y=0)$ for longitudinal scans in every step of the fitting procedure.

In order to check the validity of the theoretical calculations, two different values for the vertical resolution have been chosen, without changing any parameter of the sample and its surrounding. By narrowing the detector slit the vertical resolution has been improved by a factor of 20. As shown in Fig. 18, the improvement of the resolution suppresses the intensity of the broad component much more than the intensity of the sharp component in the center of the scan. However, applying the fitting procedure described above the fitted values for the correlation lengths and the susceptibilities were independent of the resolution width.

[1] R. Cowley, Phys. Scr., T **66**, 24 (1996).
[2] S. Andrews, J. Phys. C **19**, 3721 (1986).
[3] D. F. McMorrow, N. Hamaya, S. Shimomura, Y. Fujii, S. Kishimoto, and H. Iwasaki, Solid State Commun. **76**, 443 (1990).
[4] G. Shirane, R. Cowley, M. Matsuda, and S. Shapiro, Phys. Rev. B **48**, 15 595 (1993).
[5] K. Müller and W. Berlinger, Phys. Rev. Lett. **26**, 12 (1971).
[6] T. Riste, E. Samuelsen, K. Otnes, and J. Feder, Solid State Commun. **9**, 1455 (1971).
[7] T. R. Thurston, G. Helgesen, J. P. Hill, Doon Gibbs, B. D. Gaulin, and P. J. Simpson, Phys. Rev. B **49**, 15 730 (1994).
[8] H.-B. Neumann, U. Rütt, J. R. Schneider, and G. Shirane, Phys. Rev. B **52**, 3981 (1995).
[9] U. Rütt, A. Diederichs, J. R. Schneider, and G. Shirane, Europhys. Lett. **39**, 395 (1997).
[10] G. M. Watson, B. D. Gaulin, Doon Gibbs, T. R. Thurston, P. J. Simpson, S. M. Shapiro, G. H. Lander, H. Matzke, S. Wang, and M. Dudley, Phys. Rev. B **53**, 686 (1996).
[11] S. Wang, Y. Zhu, and S. Shapiro, Phys. Rev. Lett. **80**, 2370 (1998).
[12] R. Bouchard, D. Hupfeld, T. Lippmann, J. Neuefeind, H.-B. Neumann, H. F. Poulsen, U. Rütt, T. Schmidt, J. R. Schneider, J. Süssenbach, and M. von Zimmermann, J. Synchrotron Radiat. **5**, 90 (1998).
[13] K. Hirota, J. P. Hill, S. M. Shapiro, G. Shirane, and Y. Fujii, Phys. Rev. B **52**, 13 195 (1995).
[14] H. Scheel, J. Bednorz, and P. Dill, Ferroelectrics **13**, 507 (1976).
[15] G. Shirane and Y. Yamada, Phys. Rev. **177**, 858 (1969).
[16] S. Shapiro, J. Axe, G. Shirane, and T. Riste, Phys. Rev. B **6**, 4332 (1972).
[17] C. Darlington and O. D. A. O'Connor, J. Phys. C **9**, 3561 (1976).
[18] I. Denk, W. Münch, and J. Maier, J. Am. Ceram. Soc. **78**, 3265 (1995).
[19] J. Fleig, F. Noll, and J. Maier, Ber. Bunsenges. Phys. Chem. **100**, 607 (1996).
[20] J. MacDonald, in *Impedance Spectroscopy* (Wiley, New York, 1987), p. 79.
[21] S. Rodewald, J. Fleig, and J. Maier, J. Eur. Ceram. Soc. **19**, 797 (1999).
[22] W. Zachariasen, *Theory of X-ray Diffraction in Crystals* (Wiley, New York, 1945).
[23] B. Batterman and H. Cole, Rev. Mod. Phys. **36**, 681 (1964).
[24] J. R. Schneider, J.-E. Jørgensen, and G. Shirane, Phase Transitions **8**, 17 (1986).
[25] J. Als-Nielsen, in *Topics in Current Physics: Structure and Dynamics of Surfaces*, edited by W. Schommers and P.v. Blanckenhagen (Springer, Berlin, 1986), Vol. 2.
[26] R. Cowley, Adv. Phys. **29**, 1 (1980).
[27] D. Bäuerle and W. Rehwald, Solid State Commun. **27**, 1343 (1978).
[28] J. Hastings, S. Shapiro, and B. Frazer, Phys. Rev. Lett. **40**, 237 (1978).
[29] W. Zhong and D. Vanderbilt, Phys. Rev. B **53**, 5047 (1996).
[30] J. LeGuillou and J. Zinn-Justin, Phys. Rev. B **21**, 3976 (1980).
[31] M. Fisher, J. Math. Phys. **5**, 944 (1964).
[32] M. Altarelli, M. D. Nunez-Regueiro, and M. Papoular, Phys. Rev. Lett. **74**, 3840 (1995).
[33] Q. J. Harris, Q. Feng, R. J. Birgeneau, K. Hirota, G. Shirane, M. Hase, and K. Uchinokura, Phys. Rev. B **52**, 15 420 (1995).
[34] Michael Gofman, Joan Adler, Amnon Aharony, A. B. Harris, and Moshe Schwartz, Phys. Rev. Lett. **71**, 1569 (1993).
[35] H.-B. Neumann, U. Rütt, R. Bouchard, J. R. Schneider, and N. Nagasawa, J. Appl. Crystallogr. **27**, 1030 (1994).
[36] U. Rütt, H. B. Neumann, H. Poulsen, and J. R. Schneider, J. Appl. Crystallogr. **28**, 729 (1995).